AIAA JOURNAL
Vol. 38, No. 9, September 2000

Low-Diffusion Flux-Splitting Methods for Real Fluid Flows with Phase Transitions

Jack R. Edwards* and Randall K. Franklin†
North Carolina State University, Raleigh, North Carolina 27695
and
Meng-Sing Liou‡
NASA John H. Glenn Research Center at Lewis Field, Cleveland, Ohio 44135

Methods for extending the AUSM+ low-diffusion flux-splitting scheme toward the calculation of real fluid flows at all speeds are presented. The single-phase behavior of the fluid is defined by the Sanchez–Lacombe equation of state (Sanchez, I. C., and Lacombe, R. H., "An Elementary Molecular Theory of Classical Fluids: Pure Fluids," *Journal of Physical Chemistry*, Vol. 80, No. 21, 1976, pp. 2352–2362), a lattice-fluid description. Liquid–vapor phase transitions are modeled through a homogeneous equilibrium approach. Time-derivative preconditioning is utilized to allow effective integration of the equation system at all flow speeds and all states of compressibility. Modifications to the preconditioned variant of AUSM+ necessary to preserve solution accuracy under such conditions are presented in detail. One-dimensional results are presented for the faucet problem, a classic test case for multifluid algorithms, as well as for liquid octane flow through a converging–diverging nozzle. Two-dimensional calculations are presented for water flow over a hemisphere/cylinder geometry and liquid carbon dioxide flow through a capillary nozzle. The results illustrate the effectiveness of the flux-splitting scheme in capturing such multiphase flow features as cavitation zones and vapor–liquid condensation shocks, as well as incompressible liquid and compressible vapor responses, within the framework of a single numerical algorithm.

I. Introduction

THE utility of computational fluid dynamics (CFD) techniques in the analysis of complex engineering systems is well established, with both mathematical advances and advances in computer architectures playing a major role. Traditionally, CFD methods have been divided into two major classes, pressure-based methods, originally devised for solving the incompressible flow equations in primitive variables, and density-based methods, formulated to solve the compressible flow equations and generally developed for gasdynamic applications. Recently, the concept of time-derivative preconditioning[1–4] has been advanced to bridge this gap. Originally developed as an approach for alleviating numerical stiffness encountered in solving the compressible flow equations for low Mach numbers, preconditioning strategies have been viewed more recently as a unifying framework for flow simulation across the Mach number range. A properly designed time-derivative preconditioning method will intimately connect the numerical discretization of the Euler (inviscid) components of the Navier–Stokes set with the integration method itself, providing both high solution accuracy and numerical efficiency for flows at all speeds.

To this point, preconditioning strategies have been used primarily in gasdynamic applications, with some extensions to supercritical fluids having been proposed and tested.[5,6] The possible utility of preconditioning techniques for other situations, such as the simulation of compressible liquids, polymeric liquids, and fluids undergoing equilibrium or nonequilibrium phase change, is apparent. In such cases, the compressibility of the fluid can vary dramatically from point to point; similarly, the flow speed can also vary over a wide range. An example of a situation that encompasses some of these effects is the expansion of compressed liquid carbon dioxide (CO_2) out of the nozzle of a fire extinguisher. Within the internal flowpath, CO_2 is liquidlike in character; flow speeds are generally slow and the sound speed is large, meaning that an analysis based on the incompressible Navier–Stokes equations might be valid. During the rapid expansion process, the pressure drop forces a phase change, leading first to the gasification of the CO_2, then to the formation of particulate solid CO_2 as the temperature continues to drop. The expanding gaseous CO_2 reaches supersonic values, and normal or oblique shocks may be formed as the fluid compresses back to its ambient state. This sequence of events is extremely difficult to simulate in conventional CFD codes. The need to predict such complex phenomena in the hydrocarbons processing, spray coatings, aerospace, and automotive industries is high, and the availability of a unified CFD methodology capable of handling such situations would be greatly desired.

A starting point is the construction of upwind differencing methods capable of accurately simulating the response of fluids that may exist simultaneously in different phases. The general multiphase flow problem involves the formulation of separate transport equations for each separate phase and the development of suitable models for accounting for interphase mass, momentum, and energy transfer. The development of upwind methods for multiphase flow simulation is a current subject of research, one complicated by the lack of system hyperbolicity and the complexities of interphase transfer. Toumi[7] presents a weak formulation of Roe's approximate Riemann solver, suitable for real fluid flows. This work was later extended into a more comprehensive formulation for isothermal two-fluid flows.[8] Coquel et al.[9] have developed Boltzmann-type flux-splitting schemes for solving two-phase flow problems, whereas Tang and Huang[10] have proposed a Godunov-type approach for the gas–liquid Riemann problem. Tiselj and Petelin[11] introduce upwind differencing techniques into a version of the RELAP5 multiphase flow code. Other efforts at developing upwind schemes for the general multiphase flow problem and simplifications thereof are described by Toumi et al.[12]

The upwind methods developed in the preceding references are of significant complexity as compared with their perfect-gas counterparts. Furthermore, none truly accounts for the wide timescale variations present in many multiphase flows and, if used in concert with conventional density-based integration methods, could exhibit

Received 14 June 1999; presented as Paper 99-3327 at the AIAA 14th Computational Fluid Dynamics Conference, Norfolk, VA, 28 June–1 July 1999; revision received 23 January 2000; accepted for publication 23 January 2000.

*Assistant Professor, Department of Mechanical and Aerospace Engineering, Campus Box 7910; jredward@eos.ncsu.edu.
†Graduate Research Assistant, Department of Mechanical and Aerospace Engineering, Campus Box 7910; rkfrankl@eos. ncsu.edu.
‡Senior Scientist, Turbomachinery and Propulsion Systems Division; Meng-Sing.Liou@lerc.nasa.gov.

both slow convergence and solution inaccuracy for low-speed flows. Low-diffusion flux-splitting schemes, such as AUSM+,[13] AUSMDV,[14] and LDFSS,[15] have emerged as efficient alternatives to traditional upwind methods based on characteristic wave decomposition. Such methods have been shown to combine the high accuracy of more sophisticated techniques with the robustness and simplicity of flux-vector splitting schemes. Recent work[16] has successfully extended a class of low-diffusion flux-splitting methods to operate effectively at all speeds, with the governing premise being that the speed of sound should cease to be an important scaling parameter for the diffusive contributions to the interface flux as the Mach number becomes small. This scaling shift is accomplished through the use of the eigenvalues of the preconditioned Euler system in the flux-splitting method.

Prior efforts in the construction of low-diffusion flux-splitting schemes have assumed that the fluid behaves as an ideal gas or a mixture thereof. One purpose of this paper is to present extensions of preconditioned low-diffusion flux-splitting schemes that are valid for generalized state equations, which may describe single-phase liquid, gas, or supercritical fluid behavior of a given substance. Our attention will be focused on AUSM+, perhaps the most rigorously developed of the current techniques, but the modifications outlined herein should be valid for other low-diffusion schemes as well. A second thrust of this work is to provide an initial direction toward the development of extensions suitable for solving the general multiphase flow problem for arbitrary flow speeds and arbitrary levels of compressibility. This initial step will start with the development of a homogeneous equilibrium model for liquid–vapor phase transitions using information extracted from a generalized state equation. The resulting equations are similar to the preconditioned Euler system in structure and in mathematical character, but may admit such multiphase flow features as cavitation zones and vapor–liquid condensation shocks. Other homogeneous equilibrium models have been utilized by Toumi[7] in the simulation of boiling in a pipe, by Saurel et al.[17] for high-speed cavitating flows over projectiles, and by Yabe et al.[18] in the development of unified models for simulating liquid, solid, and gaseous flow dynamics.

II. Real Fluid State Description

A. Single-Phase Formulation

The thermodynamic state of a single-phase real fluid is defined by the relations $p = p(\rho, T)$ and $h = h(\rho, T)$. In the present work, we utilize the Sanchez–Lacombe equation of state,[19] a lattice-fluid description valid for high-molecular-weight liquids.[20] The Sanchez–Lacombe equation behaves similarly to cubic equations of state, such as the Van der Waals equation or the Peng–Robinson[20] equation, but offers better predictive capability for polar substances (such as water) far from their critical point. The methods outlined subsequently have also been used with the Peng–Robinson equation; details can be found in Refs. 21 and 22.

The Sanchez–Lacombe equation of state[19] is given by

$$\bar{p} = -(\bar{\rho}^2 + \bar{T}\{\ell n(1 - \bar{\rho}) + \bar{\rho}[1 - (1/r_\bullet)]\}) \tag{1}$$

where

$$\bar{p} = p/p_\bullet \tag{2}$$

$$\bar{\rho} = \rho/\rho_\bullet \tag{3}$$

$$\bar{T} = T/T_\bullet \tag{4}$$

$$r_\bullet = p_\bullet M_w/\rho_\bullet R T_\bullet \tag{5}$$

where R is the universal gas constant and M_w is the fluid molecular weight. The reference values $p_\bullet$, $\rho_\bullet$, and $T_\bullet$ are generally determined for a particular fluid by least-squares fitting of experimental liquid-state density and vapor pressure data. Allowable density values are from zero to slightly less than $\rho_\bullet$ ($0 \le \bar{\rho} < 1$); values outside these bounds fall out of the range of validity of the equation. Physical critical-point properties are not used explicitly in the Sanchez–Lacombe formulation, as the mean-field approximation utilized in its derivation breaks down near the critical point. Numerical values for the critical-point properties as determined by the equation of state can be determined by straightforward differentiation,[19] with the results being

$$\bar{\rho}_c = 1\Big/\left(1 + \sqrt{r_\bullet}\right) \tag{6}$$

$$\bar{T}_c = 2r_\bullet \bar{\rho}_c^2 \tag{7}$$

$$\bar{p}_c = p_c(\bar{\rho}_c, \bar{T}_c) \tag{8}$$

Table 1 summarizes Sanchez–Lacombe reference values for water, octane, and carbon dioxide.

Table 1 Sanchez–Lacombe[19] reference values

Fluid	$T_\bullet$, K	$p_\bullet$, Pa	$\rho_\bullet$, kg/m^3
Water	613.8	2846.9*e*6	1150.5
Octane	504.1	317.0*e*6	835.1
Carbon dioxide	283.0	658.9*e*6	1622.0

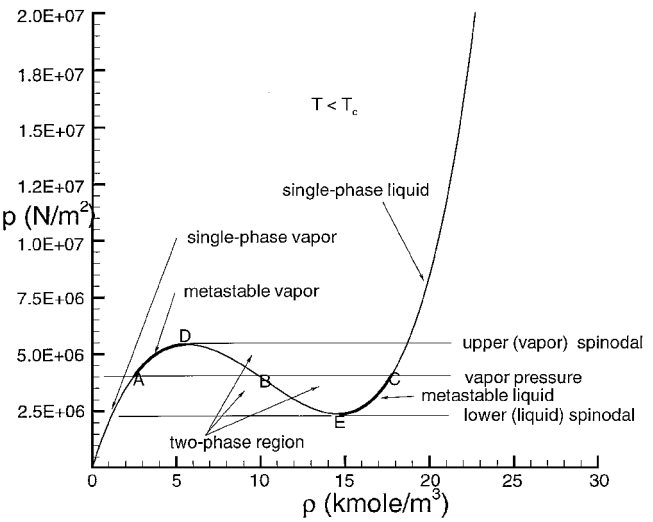

Fig. 1 Pressure vs molar density (isotherm below critical temperature).

A pressure–density isotherm for a temperature below the critical temperature is plotted in Fig. 1 for the Sanchez–Lacombe equation.[19] Clearly indicated is the vapor regime, where pressure varies nearly linearly with density, and the liquid regime, where large pressure changes are required to induce a density change. For a given pressure and temperature, the solution of Eq. (1) returns one or three values of the density. The former corresponds to the single-phase region, whereas the latter corresponds to the two-phase region, where vapor and liquid may exist simultaneously. Because of the presence of the natural logarithm in Eq. (1), an iterative process is required to determine the densities. This is in contrast with cubic equations of state, for which an analytic approach is available.[20,21] The corresponding densities for a pressure within the two-phase region are shown as points A, B, and C. A and C represent saturated vapor and liquid states, whereas B is physically meaningless. For a particular temperature, the two-phase region is bounded by the pressure values at D and E, which are local extrema. The loci of these pressure values for temperatures between the triple and critical points define liquid and vapor spinodal curves, dividing the two-phase region into metastable vapor, unstable, and metastable liquid regions. At a particular pressure between the liquid and vapor spinodal points, the system is in equilibrium, with the vapor and liquid fugacities (or Gibbs energies) attaining equal values. This pressure is known as the vapor pressure p_v and is calculated as a function of temperature for the Sanchez–Lacombe equation[19] by solving the vapor–liquid equilibria equation

$$G(\bar{\rho}_v, \bar{T}, \bar{p}) = G(\bar{\rho}_l, \bar{T}, \bar{p}) \tag{9}$$

where the normalized Gibbs energy is expressed as

$$G = (1/\bar{\rho})\{-\bar{\rho}^2 + \bar{p} + \bar{T}[(1 - \bar{\rho})\ell n(1 - \bar{\rho}) + (\bar{\rho}/r_\bullet)\ell n\bar{\rho}]\} \tag{10}$$

The thermodynamic state description for the single-phase fluid is completed by the specification of enthalpy departure functions,[23] which introduce a density dependence into the enthalpy description and, thus, account for latent heat effects. For the Sanchez–Lacombe equation,[19] the enthalpy per unit mass of the fluid may be expressed as

$$h(\rho, T) = h_I(T) - (p_*/\rho_*)(2\bar{\rho} + \bar{T}\{[\ln(1-\bar{\rho})/\bar{\rho}] + 1\}) \quad (11)$$

where $h_I(T)$ is the enthalpy per unit mass of an ideal gas at the same temperature (determined from curve fits presented by McBride et al.[24]).

The physical sound speed of the fluid can be calculated from thermodynamic considerations; a more useful CFD analog is the acoustic eigenvalue, which may be obtained by determining the eigenvalues of the Jacobian matrix $(\partial \boldsymbol{W}/\partial \boldsymbol{U})$ $(\partial \boldsymbol{F}/\partial \boldsymbol{W})$, where $\boldsymbol{F}$ is an Euler flux vector closed according to the general expressions $p = p(\rho, T)$ and $\rho h = \rho h(\rho, T)$; $\boldsymbol{U}$ is the vector of conserved variables; and $\boldsymbol{W}$ is the vector of primitive variables $[\rho, u, v, w, T]^T$. The choice of ρh (rather than h) and the choices of density and temperature as independent variables are dictated by the equilibrium description of the flow in the two-phase region, as described later. For this choice of variables, the effective sound speed is given by

$$a^2 = \frac{(\rho h)_T p_\rho - p_T[(\rho h)_\rho - h]}{(\rho h)_T - p_T} \quad (12)$$

B. Homogeneous Equilibrium Two-Phase Flow Model

The Sanchez–Lacombe equation[19] gives no useful information in the unstable parts of the two-phase region. For densities between the spinodal values, it can be shown that the acoustic eigenvalues are complex, meaning that the Euler system is not hyperbolic in time and that conventional time-marching procedures for integrating the equations are ill posed. Note that the liquid spinodal pressure may be negative for high-molecular-weight liquids at lower temperatures, implying that the simulated expansion of a liquid might produce reasonable densities, but unphysical pressures, in the metastable region.

One means of avoiding these difficulties starts with the introduction of a void-fraction formalism for the two-phase region and the assumption of thermodynamic and kinematic equilibrium between the phases. For an equilibrium two-phase flow, the vapor pressure $p_v(T)$ is directly related to the temperature through the Clausius–Clapyron equation, and the density and temperature are independent variables. Given updated values for the density and temperature at a grid point as determined from a time-integration method, the following procedure is performed:

1) Determine the vapor pressure at that temperature and establish the saturation densities $\rho_l(T)$ and $\rho_v(T)$ and the saturation enthalpies $h_l(T)$ and $h_v(T)$. Because this determination is expensive, we solve the vapor–liquid equilibria equation (9) over a relevant range of temperatures using a separate program and tabulate the results for vapor pressure, saturation density, and saturation enthalpy as a function of discrete temperature values. Linear interpolation is then used to extract the local values from Table 1 given the updated temperature.

2) If the fluid density is between the saturation values, the equilibrium equation of state for the homogeneous mixture of liquid and vapor is given by

$$p = p_v(T) \quad (13)$$

$$\rho h(\rho, T) = \rho_v(T)\alpha_v(\rho, T)h_v(T) + \rho_l(T)\alpha_l(\rho, T)h_l(T) \quad (14)$$

$$\alpha_v(\rho, T) = \frac{\rho - \rho_l(T)}{\rho_v(T) - \rho_l(T)} \quad (15)$$

$$\alpha_l(\rho, T) = 1 - \alpha_v \quad (16)$$

3) If the density is not between the saturation values or the temperature is greater than the critical temperature, then the single-phase description given by the equation of state is used to determine the pressure and enthalpy.

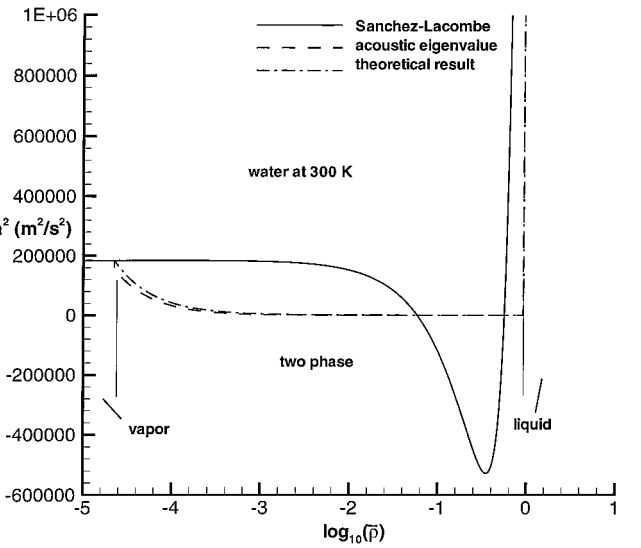

Fig. 2 Reduced density vs a^2 (water at 300 K).

In this description, the saturation-state values are strict functions of temperature; density dependence is introduced through the void fractions α, and latent-heat effects arise through the change in departure enthalpy between the saturation states. The thermodynamic derivatives p_ρ, p_T, $(\rho h)_\rho$, and $(\rho h)_T$ needed in the time-integration method and in the sound speed definition can be computed by straightforward differentiation of the given expressions. These are discontinuous at phase transition points, leading to dramatic changes in the effective sound speed in the two-phase region. Figure 2 plots a^2 as a function of the reduced density $\bar{\rho}$ for both the Sanchez–Lacombe equation[19] and the Sanchez–Lacombe equation augmented by the homogeneous equilibrium model (13–16). The fluid is water at a temperature of 300 K. As shown, the equilibrium two-phase description preserves a real value for the sound speed, whereas the basic Sanchez–Lacombe equation results in negative values for a^2. Also shown is a theoretical result for the sound speed in a homogeneous two-phase mixture of liquid and vapor[25]:

$$1/\rho a^2 = \left[\alpha_v \middle/ \rho_v a_v^2(T)\right] + \left[\alpha_l \middle/ \rho_l a_l^2(T)\right] \quad (17)$$

where $a_{v,l}^2(T)$ are obtained from Eq. (12) evaluated at the saturation states $\rho_{v,l}(T)$. The eigenvalue calculation for a^2 agrees reasonably well with the theoretical estimate except near single-phase/two-phase junctures, where the latter blends smoothly with the saturation-state values and the former exhibits a jump discontinuity. The theoretical expression for the sound speed is numerically more robust and is used in most of the calculations presented herein. Both expressions result in very small values (on the order of meters per second) for the sound speed near the liquid-phase/two-phase interface, meaning that a shift to a locally supersonic flow condition during a phase transition is a distinct possibility.

The preceding formulation neglects velocity-slip effects and is related to that described in Refs. 7 and 17. This system is hyperbolic in character and is similar to the Euler system in structure but admits such multiphase features as cavitation zones and condensation shocks. A key element is the use of density and temperature as the working thermodynamic variables, particularly in contrast with typical low-speed formulations, which utilize pressure and temperature as the working thermodynamic variables. This choice is driven by the equilibrium closure for the two-phase region, in which pressure and temperature are not independent variables.

III. Time-Derivative Preconditioning

The utility of time-derivative preconditioning in the solution of the real fluid system described lies in its ability to provide a smooth transition between nearly incompressible conditions (such as liquid-phase or low-Mach-number vapor or supercritical-fluid-phase flows) and strongly compressible conditions (such as two-phase flows or high-speed vapor phase flows). As in previous

work,[16] the real fluid extension utilizes the preconditioner of Weiss and Smith,[4] a variant of the Choi–Merkle[2]/Turkel[1] family of preconditioners. This preconditioner may be expressed as a rank-one perturbation of the Jacobian matrix $\partial \boldsymbol{U}/\partial \boldsymbol{W}$. The time-derivative term in the real fluid Euler system is replaced by

$$\Gamma \frac{\partial \boldsymbol{W}}{\partial t} \equiv \left(\frac{\partial \boldsymbol{U}}{\partial \boldsymbol{W}} + \Theta \boldsymbol{u} \boldsymbol{v}^T \right) \frac{\partial \boldsymbol{W}}{\partial t} \tag{18}$$

where

$$\boldsymbol{u} = [1, u, v, w, H]^T \tag{19}$$

$$\boldsymbol{v} = [p_\rho, 0, 0, 0, p_T]^T \tag{20}$$

$$\Theta = \left(1/V_*^2\right) - (1/a^2) \tag{21}$$

H is the total enthalpy per unit mass, and a is the acoustic speed defined earlier. The reference velocity V_* is defined as

$$V_*^2 = \min\left[a^2, \max\left(|\boldsymbol{V}|^2, V_\infty^2\right)\right] \tag{22}$$

where $|\boldsymbol{V}|$ is the local fluid velocity magnitude and V_∞ is a user-specified cutoff velocity designed to prevent singular behavior at stagnation conditions. At low speeds, this preconditioner essentially replaces the physical thermodynamic derivative ρ_p with $1/V_*^2$, rescaling the eigenvalues of the Euler system so that the condition number remains bounded. The eigenvalues of $\Gamma^{-1}A$ ($A = \partial F/\partial W$) are u and $u' \pm a'$, where u is the velocity component in the x direction and

$$u' \pm a' = \tfrac{1}{2}\left[\left(1 + M_*^2\right)u \pm a\sqrt{\left(1 - M_*^2\right)^2 M^2 + 4M_*^2} \right] \tag{23}$$

$$M_*^2 = V_*^2/a^2 \tag{24}$$

$$M = u/a \tag{25}$$

In contrast to the real fluid description of Ref. 6, where other terms in the Jacobian $\partial \boldsymbol{U}/\partial \boldsymbol{W}$ are rescaled according to other criteria, these eigenvalues have the same form as their perfect-gas counterparts, with the perfect-gas sound speed simply replaced by the real fluid description.

IV. Modifications to AUSM+ for Real Fluid Flows

A framework for extending low-diffusion flux-splitting methods, such as AUSM+, AUSMDV, and LDFSS, to operate effectively in conjunction with time-derivative preconditioning has been proposed in Ref. 16. These methods reduce to a standard upwind formulation at sonic transitions, preserving the discontinuity-capturing traits of the methods, but recover viable discretizations of the incompressible flow equations as the Mach number approaches zero. Given the structural similarity between the Euler system closed according to the equilibrium real fluid state description and the perfect-gas Euler system, it is anticipated that modifications to low-diffusion upwind schemes to enable accurate capturing of real fluid phenomena should be relatively straightforward. In this paper, we concentrate on AUSM+, but the techniques as proposed should be valid for other flux-splitting concepts.

In the following, a review of preconditioned AUSM+ is presented, followed by modifications necessary to progress toward a formulation valid for general fluids at all speeds. The inviscid interface flux $\boldsymbol{F}_{i+1/2}$ in the x direction is split into a convective contribution $\boldsymbol{F}^c_{1/2}$ plus a pressure contribution $\boldsymbol{F}^p_{1/2}$, which are treated separately. The convective flux is defined as

$$\boldsymbol{F}^c_{\frac{1}{2}} = \dot{m}_{\frac{1}{2}} \begin{bmatrix} 1 \\ u \\ v \\ w \\ H \end{bmatrix}_{i/i+1} \tag{26}$$

where state i is chosen for the column vector $(1, u, v, w, H)^T$ if $\dot{m}_{1/2}$ is nonnegative and state $i+1$ is chosen if $\dot{m}_{1/2}$ is negative. The pressure flux is defined as

$$\boldsymbol{F}^p_{\frac{1}{2}} = \begin{bmatrix} 0 \\ p_{\frac{1}{2}} \\ 0 \\ 0 \\ 0 \end{bmatrix} \tag{27}$$

A. Mass Flux Splitting

The interface mass flux $\dot{m}_{1/2}$ is expressed in terms of sets of polynomials in Mach number, defined as

$$M_i = u_i/\tilde{a}_{\frac{1}{2}} \tag{28}$$

where $\tilde{a}_{1/2}$ is a preconditioned speed of sound, evaluated at the cell interface. The preconditioned sound speed is based on the eigenvalues of the preconditioned equation system and is defined as

$$\tilde{a}_{\frac{1}{2}} = f_{\frac{1}{2}} a_{\frac{1}{2}} \tag{29}$$

where

$$f_{\frac{1}{2}} = \frac{\sqrt{\left(1 - M_*^2\right)^2 M^2 + 4M_*^2}}{\left(1 + M_*^2\right)} \tag{30}$$

The $\frac{1}{2}$ notation represents an arithmetic average in general. The one exception is the interface sound speed, which is defined as

$$a_{\frac{1}{2}} = \sqrt{\frac{(\rho a^2)_{\frac{1}{2}}}{\rho_{\frac{1}{2}}}} \tag{31}$$

This density-weighted average seems to perform better in capturing phase interfaces. The overall evaluation of $\tilde{a}_{1/2}$ is an example of the use of a numerical speed of sound in a flux formula to achieve certain numerical properties.[26] In this case, the numerical sound speed $\tilde{a}_{1/2}$ facilitates a reduction to a discretization suitable for essentially incompressible flows. Other uses of the concept may be found in Ref. 26.

Two sets of polynomials are required to define the mass flux:

$$\mathcal{M}^{\pm}_{(1)} = \tfrac{1}{2}(M \pm |M|) \tag{32}$$

$$\mathcal{M}^{\pm}_{(4)} = \begin{cases} \pm\frac{1}{4}(M \pm 1)^2 \pm \frac{1}{8}(M^2 - 1)^2, & |M| < 1 \\ \mathcal{M}^{\pm}_{(1)}, & \text{otherwise} \end{cases} \tag{33}$$

The numerals in the subscripts of $\mathcal{M}$ indicate the degree of the polynomials. With these, the interface mass flux is defined as

$$\dot{m}_{\frac{1}{2}} = \tilde{a}_{\frac{1}{2}}\left(\rho_i m^+_{\frac{1}{2}} + \rho_{i+1} m^-_{\frac{1}{2}} + \dot{m}_p \right) \tag{34}$$

$$m^{\pm}_{\frac{1}{2}} = \tfrac{1}{2}\left(m_{\frac{1}{2}} \pm \left| m_{\frac{1}{2}} \right| \right) \tag{35}$$

$$m_{\frac{1}{2}} = \mathcal{M}^+_{(4)}(M_i) + \mathcal{M}^-_{(4)}(M_{i+1}) \tag{36}$$

The pressure-diffusion contribution to the interface mass flux $\dot{m}_p$ arises from the need to couple the pressure and velocity fields at low Mach number. This term is defined as

$$\dot{m}_p = \left(\frac{1}{M_*^2} - 1 \right) \mathcal{M}_{\frac{1}{2}} \frac{p_i - p_{i+1}}{p_i/\rho_i + p_{i+1}/\rho_{i+1}} \tag{37}$$

$$\mathcal{M}_{\frac{1}{2}} = \mathcal{M}^+_{(4)}(M_i) - \mathcal{M}^+_{(1)}(M_i) - \mathcal{M}^-_{(4)}(M_{i+1}) + \mathcal{M}^-_{(1)}(M_{i+1}) \tag{38}$$

in Ref. 16.

For nearly incompressible flows ($\rho \approx$ const and $a^2 \gg |V|^2$), the pressure diffusion contribution can be approximated as

$$\dot{m}_p \approx \frac{C_{\frac{1}{2}}}{2} \frac{\rho_{\frac{1}{2}} a_{\frac{1}{2}}^2}{p_{\frac{1}{2}}} \frac{\sqrt{u_{\frac{1}{2}}^2 + 4V_*^2}}{V_*^2} (p_i - p_{i+1}) \tag{39}$$

The function $C_{1/2}$ is of order unity. The coefficient $\rho_{1/2} a_{1/2}^2 / p_{1/2}$ is also of order unity for gases, but for liquids and supercritical fluids governed by generalized state equations, the coefficient may become much larger than unity. This represents an unphysical source of numerical diffusion for liquid-state calculations, one eliminated by redefining the pressure-diffusion contribution as

$$\dot{m}_p = \frac{1}{2}\left(\frac{1}{M_*^2} - 1\right) \mathcal{M}_{\frac{1}{2}} \frac{p_i - p_{i+1}}{a_{\frac{1}{2}}^2} \tag{40}$$

The mass flux in the incompressible limit ($\rho =$ const and $a \approx \infty$) becomes

$$\dot{m}_{\frac{1}{2}} = \rho \left[u_{\frac{1}{2}} + \tfrac{1}{2}\left(M_{\frac{1}{2}}^I\right)^3 (u_i - u_{i+1}) \right]$$

$$+ \tfrac{1}{2} \mathcal{M}_{\frac{1}{2}}\left(M_i^I, M_{i+1}^I\right)\left(\sqrt{u_{\frac{1}{2}}^2 + 4V_*^2} \Big/ V_*^2\right)(p_i - p_{i+1}) \tag{41}$$

where $M_{i,i+1}^I$ and $M_{1/2}^I$ are derived from Eq. (28) by neglecting M_*^2 relative to unity,

$$M_{i,i+1}^I = \frac{u_{i,i+1}}{\sqrt{u_{\frac{1}{2}}^2 + 4V_*^2}} \tag{42}$$

$$M_{\frac{1}{2}}^I = \tfrac{1}{2}\left(M_i^I + M_{i+1}^I\right)$$

$$= u_{\frac{1}{2}} \Big/ \sqrt{u_{\frac{1}{2}}^2 + 4V_*^2} \tag{43}$$

As shown, the limiting form of the mass flux consists of three elements: a term proportional to the cell-average velocity $u_{1/2}$, a diffusive component proportional to the velocity difference $u_i - u_{i+1}$, and the pressure diffusion term, which scales as the inverse of the reference velocity. Unlike that proposed in Ref. 16, this mass flux expression is independent of the thermodynamic state description and will apply equally well to incompressible liquids and gases.

B. Pressure Flux Splitting

The pressure flux-splitting techniques used in AUSM-type algorithms have their genesis in that proposed originally by Van Leer[27] for perfect gases and extended further by Liou and Steffen[28] and Liou.[13] As shown in Ref. 16, these techniques result in scaling problems for low-Mach-number, perfect-gas applications. This paper contends that such scaling problems persist for real fluid applications and that they can only be completely resolved by developing a new form of the pressure flux splitting.

We consider the interface pressure as defined as

$$p_{\frac{1}{2}} = \mathcal{P}^+(M_i) + \mathcal{P}^-(M_{i+1}) \tag{44}$$

For $M \geq 1$, $\mathcal{P}^+ = p_i$ and $\mathcal{P}^- = 0$, whereas for $M \leq -1$, $\mathcal{P}^+ = 0$ and $\mathcal{P}^- = p_{i+1}$. This results in upwinding of the pressure flux for supersonic Mach numbers. For subsonic Mach numbers, we express $\mathcal{P}^{\pm}$ as follows:

$$\mathcal{P}^+(M_i) = \tfrac{1}{2}[1 + e(M_i)]p_i$$

$$\mathcal{P}^-(M_{i+1}) = \tfrac{1}{2}[1 - e(M_{i+1})]p_{i+1} \tag{45}$$

The first-degree polynomial proposed by Liou and Steffen[28] has

$$e(M) = M \tag{46}$$

whereas the general α polynomial proposed by Liou[13] has

$$e(M) = \left(\tfrac{3}{2} + 2\alpha\right)M - \left(\tfrac{1}{2} + 4\alpha\right)M^3 + 2\alpha M^5 \tag{47}$$

The third-degree Van Leer pressure splitting[27] corresponds to $\alpha = 0$, whereas the fifth-degree polymomial used in AUSM+ has $\alpha = \frac{3}{16}$.

Let us consider a modified form for the pressure splitting family such that the higher-degree contributions are linearized about an average Mach number $M_{1/2} = (M_i + M_{i+1})/2$:

$$\mathcal{P}^+ = \tfrac{1}{2}\left[1 + e\left(M_{\frac{1}{2}}\right) + e(M_i) - e\left(M_{\frac{1}{2}}\right)\right]p_i$$

$$\mathcal{P}^- = \tfrac{1}{2}\left[1 - e\left(M_{\frac{1}{2}}\right) + e\left(M_{\frac{1}{2}}\right) - e(M_{i+1})\right]p_{i+1} \tag{48}$$

Using a first-order Taylor expansion, this can be approximated as

$$\mathcal{P}^+ = \tfrac{1}{2}\left[1 + e\left(M_{\frac{1}{2}}\right) + \tfrac{1}{2}e'\left(M_{\frac{1}{2}}\right)(M_i - M_{i+1})\right]p_i$$

$$\mathcal{P}^- = \tfrac{1}{2}\left[1 - e\left(M_{\frac{1}{2}}\right) + \tfrac{1}{2}e'\left(M_{\frac{1}{2}}\right)(M_i - M_{i+1})\right]p_{i+1} \tag{49}$$

where

$$e' = \frac{\mathrm{d}e}{\mathrm{d}M} \tag{50}$$

With this reformulation, the first-degree pressure splitting is exactly recovered. The higher-degree splittings are not precisely recovered due to the linearization.

The sum $\mathcal{P}^+ + \mathcal{P}^-$ can then be expanded into central plus diffusive contributions:

$$\mathcal{P}^+ + \mathcal{P}^- = \tfrac{1}{2}(p_i + p_{i+1}) + \tfrac{1}{2}e\left(M_{\frac{1}{2}}\right)(p_i - p_{i+1})$$

$$+ \tfrac{1}{2}e'\left(M_{\frac{1}{2}}\right)p_{\frac{1}{2}}(M_i - M_{i+1}) \tag{51}$$

where $p_{1/2} = (p_i + p_{i+1})/2$. The advantage of the linearized formulation is that the diffusive contribution proportional to the pressure difference is completely separated from the contribution proportional to the Mach number (or velocity) difference. This allows each component to be scaled independently.

Edwards and Liou[16] showed that the contribution $p_{1/2}(M_i - M_{i+1})$ could become excessively large in the incompressible limit, as

$$p_{\frac{1}{2}}(M_i - M_{i+1}) \approx (1/\gamma)\rho_{\frac{1}{2}} a_{\frac{1}{2}}(u_i - u_{i+1}) \tag{52}$$

and the sound speed is much larger than the velocity components. This leads to over-diffusive, physically incorrect solutions as the Mach number approaches zero. A solution was found by multiplying the contribution $p_{1/2}(M_i - M_{i+1})$ by M_*^2, evaluated at the cell interface, and by defining M_i and M_{i+1} using the numerical sound speed $\tilde{a}_{1/2}$ [as in Eq. (28)]:

$$p_{\frac{1}{2}}(M_i - M_{i+1}) \approx \rho_{\frac{1}{2}} V_*^2 \left(\frac{p_{\frac{1}{2}}}{\rho_{\frac{1}{2}} a_{\frac{1}{2}}^2}\right)\frac{(u_i - u_{i+1})}{\tilde{a}_{\frac{1}{2}}} \tag{53}$$

For gases, $p_{1/2}/(\rho_{1/2} a_{1/2}^2)$ is of order unity, but as mentioned in the last section, the term can become much less than unity for real fluids. This means that the diffusive term will provide no contribution in the incompressible limit. To rectify this scaling problem, one exactly opposite to that discussed in the last section, we multiply the second diffusive term in Eq. (51) by

$$f_p = M_*^2 \frac{\rho_{\frac{1}{2}} a_{\frac{1}{2}}^2}{p_{\frac{1}{2}}} \tag{54}$$

effectively eliminating the dependence on the cell-averaged pressure. The final linearized form for the subsonic pressure splitting is as follows:

$$\mathcal{P}^+ = \tfrac{1}{2}\left[1 + e\left(M_{\frac{1}{2}}\right) + (f_p/2)e'\left(M_{\frac{1}{2}}\right)(M_i - M_{i+1})\right]p_i$$

$$\mathcal{P}^- = \tfrac{1}{2}\left[1 - e\left(M_{\frac{1}{2}}\right) + (f_p/2)e'\left(M_{\frac{1}{2}}\right)(M_i - M_{i+1})\right]p_{i+1} \tag{55}$$

The resulting interface pressure in the incompressible limit becomes

$$p_{\frac{1}{2}} = \frac{1}{2}(p_i + p_{i+1}) + \frac{1}{2}e\left(M^I_{\frac{1}{2}}\right)(p_i - p_{i+1}) + \frac{1}{2}\frac{\rho V_*^2}{\sqrt{u^2_{\frac{1}{2}} + 4V_*^2}}e'\left(M^I_{\frac{1}{2}}\right)(u_i - u_{i+1}) \tag{56}$$

Although somewhat more complicated, these linearized splittings provide a consistent scaling independent of the flow speed. Scaling inconsistencies due to differing thermodynamic state descriptions are also removed.

C. Higher-Order Extension

To extend the scheme just outlined to second-order spatial accuracy, we utilize minmod- or Van Leer-limited interpolations of the primitive-variable vector $[\rho, u, v, w, T]^T$ to the $i + \frac{1}{2}$ interface. Because the state description is quite complex and expensive to calculate, some simplifications are employed. Only the pressure and enthalpy are determined from the interpolated density and temperature. The more expensive sound speed calculation is not performed as part of this interpolation because the averages indicated in the definitions of $a_{1/2}$, $f_{1/2}$, and f_p are second order even if only nodal, rather than interpolated, data are used.

V. Applications

The techniques outlined in earlier sections, extended to generalized coordinates, have been incorporated into an implicit Navier–Stokes solver[29] suitable for calculations on multiblock domains. The Euler components of the Navier–Stokes system are discretized as indicated in preceding sections, whereas central differences are used for the viscous contributions. Surface tension effects have been neglected for the calculations presented herein. To minimize modifications to the code and to facilitate possible changes in the state description, the thermodynamic derivatives p_ρ, p_T, $(\rho h)_\rho$, and $(\rho h)_T$ are computed and stored as arrays, then used as needed in the construction of the Jacobian matrices. Viscosity and thermal conductivity data for the single-phase regions are taken from Refs. 30 and 31. For the two-phase region, it is assumed that the mixture viscosity and thermal conductivity can be expressed as void-fraction weighted averages of the saturation-state values. Turbulent effects are handled by the Spalart–Allmaras one-equation model.[32] A quasi-one-dimensional Euler solver has also been written to test basic attributes of the approach. The test cases hereafter illustrate some general features of the techniques.

A. Faucet Problem

The faucet problem[33] is a classic test case for two-fluid codes. In the present context, the fluid is taken to be liquid octane in kinematic and thermodynamic equilibrium with its vapor at a temperature of 350 K and a vapor pressure of 2061 Pa. The calculation extends over a one-dimensional domain of 12 m, with the inflow conditions specified by the temperature, the void fraction of octane vapor (taken as 0.2), and the velocity of the stream (taken as 10 m/s). The solution is forced by a gravity vector aligned in the direction of the flow, leading to acceleration of the fluid and an increase in the vapor-phase void fraction as the density decreases. A steady solution is obtained over time, with the transient response being the propagation of a discontinuous void wave downstream. With the present closure for the two-phase region, the flow is supersonic, because the effective sound speed is much smaller than the 10-m/s velocity. As such, all variables are fixed at the inflow boundary, all are extrapolated from the interior at the outflow boundary, and time-derivative preconditioning is inactive. Figure 3 compares calculation results for the void wave profile at a particular instance in time with an analytic solution for the two-fluid problem.[9] A two-stage total variation diminishing Runge–Kutta integration method[34] is used, and the solutions are advanced at a time step of 0.0015 s [corresponding approximately to a Courant–Friedrichs–Lewy (CFL) of 0.25 based on the initial velocity]. As shown, the first-order upwind scheme results in a rather diffuse prediction of the void wave profile. The second-order minmod- and Van Leer-limited extensions provide much sharper predictions, but both tend to smooth out the peak in the profile.

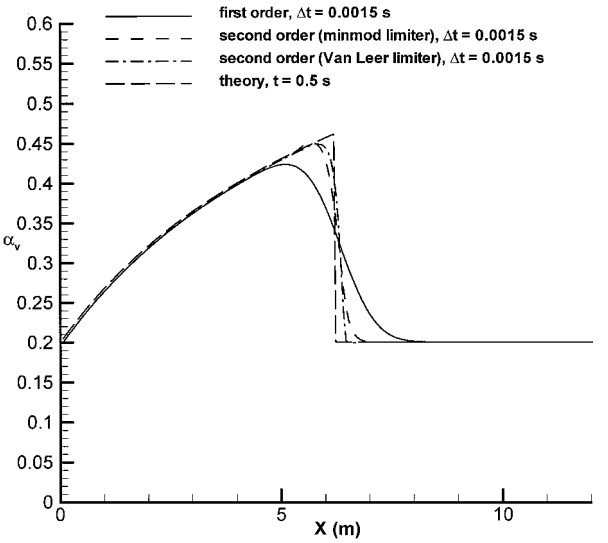

Fig. 3 Octane vapor void fraction vs x (time = 0.75 s).

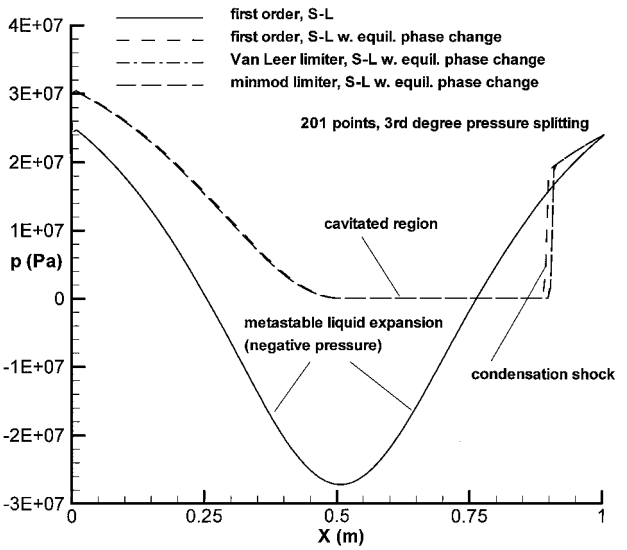

Fig. 4 Pressure vs x: expanding liquid octane.

B. Quasi-One-Dimensional Octane Expansion

The next test case considers the flow of initially liquid octane through a converging–diverging nozzle defined by the area relationship

$$A(x) = 1 + 4\left(x - \tfrac{1}{2}\right)^2, \qquad 0 \le x \le 1 \tag{57}$$

The initial conditions are $p = 4 \times 10^7$ Pa, $T = 300$ K, and $u = 10$ m/s, with the nozzle exit pressure set to 0.7 times the initial pressure level. This problem mimics a cavitating flow in that the pressure drop experienced as the flow accelerates through the nozzle throat is steep enough to force a transition to the vapor phase. The fixed exit pressure forces a recompression back to the liquid state, simulating the collapse of a cavitation region. Figure 4 presents pressure distributions for the Sanchez–Lacombe state description[19] alone and augmented by the equilibrium two-phase flow model. As shown, the pressure level in the throat lowers to unphysical levels for the unmodified Sanchez–Lacombe equation, representing a progression into the metastable liquid region. The equation system remains hyperbolic, however, as the density does not drop below the liquid spinodal value. In contrast, the pressure level for the Sanchez–Lacombe equation with the equilibrium two-phase flow model lowers to the vapor pressure of octane. This results in the generation

Table 2 Flow conditions for case C

K	T_∞, K	P_∞, Pa	U_∞, m/s
0.8	300	11,492	4.317
0.4	300	7,545	4.317
0.3	300	6,557	4.317
0.2	300	5,566	4.317

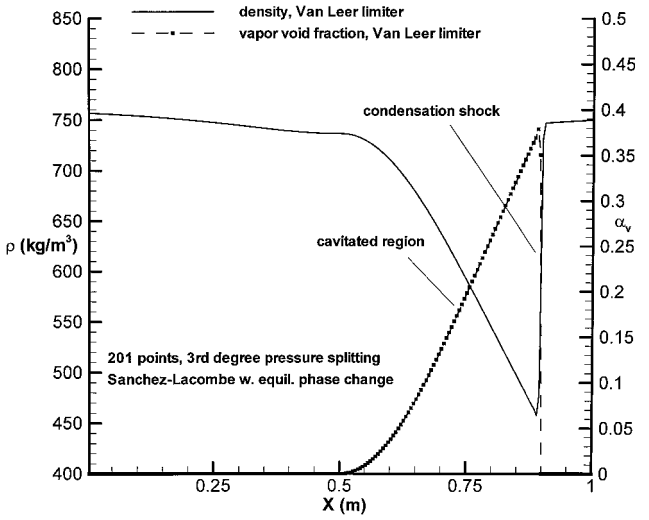

Fig. 5 Density and vapor void fraction vs x: expanding liquid octane.

of a vapor phase and a decrease in the fluid density (Fig. 5). As expected, the liquid octane density varies little in the convergent section of the nozzle. The shock-like recompression of the two-phase fluid back to the liquid state is captured monotonically by the discretization (using the third-degree Van Leer pressure splitting[27]). Other choices for the pressure splitting (not shown) give similar results. Some effects of the higher-order extensions can be seen in the positioning of the condensation shock, but otherwise, differences are slight.

C. Liquid Water Flow over a Hemisphere/Cylinder Geometry

The third test case corresponds to an experiment conducted by Rouse and McNown,[35] involving liquid water flow over a hemisphere/cylinder geometry. The data consist of surface pressure distributions, which are parameterized as functions of a cavitation number defined as

$$K = \frac{p_\infty - p_v}{\frac{1}{2}\rho_\infty U_\infty^2} \tag{58}$$

if gravitational effects are neglected. The experiments of Rouse and McNown have been widely used in the assessment of incompressible flow models for cavitation prediction.[36–38] The present compressible flow model utilizes the Sanchez–Lacombe[19] description of water, which results in a slight overprediction of the saturated liquid density (1061 vs 996 kg/m^3) at standard conditions. The grid contains 217 × 85 nodes, clustered tightly to the body surface and to the region downstream of the end of the hemispherical section, where cavity growth is expected. Initial conditions for each case are determined from an assumed Reynolds number per inch value of 1.36×10^5 (used in Refs. 37 and 38), an assumed temperature of 300 K, and the cavitation number. The results are summarized in Table 2. Under these conditions, the Sanchez–Lacombe equation[19] predicts a vapor pressure of 3589 Pa. Standard subsonic inflow (fixed velocity and temperature and extrapolated pressure) and subsonic outflow (fixed pressure and extrapolated velocity and temperature) are used in the calculations. Turbulent flow is assumed, with the Spalart–Allmaras model[32] used to determine the eddy viscosity field.

Figure 6 illustrates the effects of discretization accuracy on surface pressure predictions for $K = 0.8$, a noncavitating case, and $K = 0.4$, a cavitating case. The abscissa variable s/d is the surface

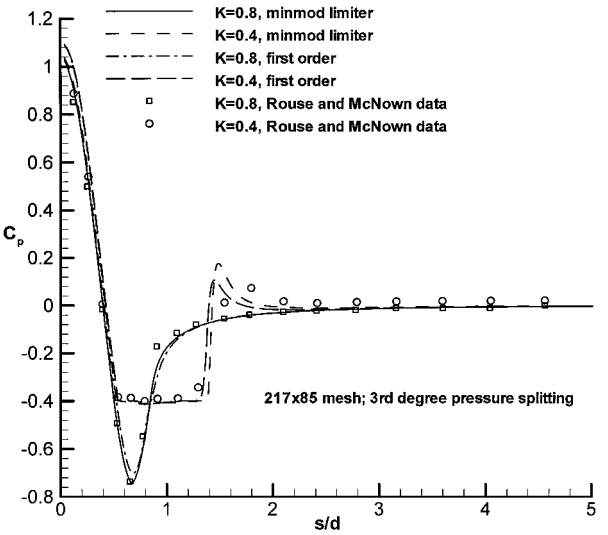

Fig. 6 Surface pressure distributions: $K = 0.4$ and 0.8.

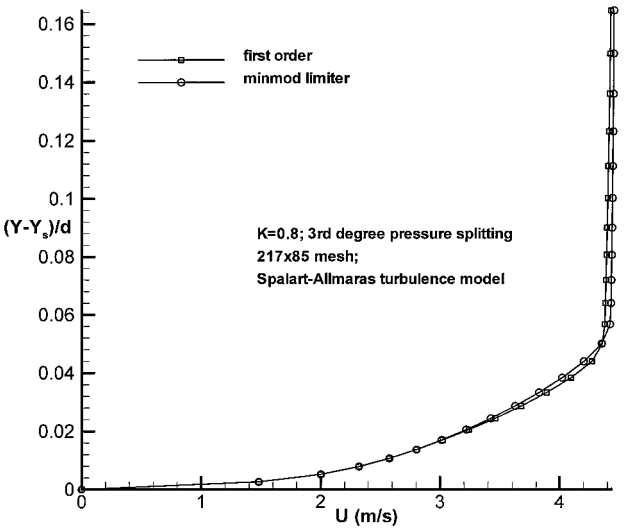

Fig. 7 Velocity profile predictions: $K = 0.8$, $s/d = 1.5$.

distance starting from the nose, normalized by the cylinder diameter of 1 in., and the ordinate variable is the pressure coefficient

$$C_p = \frac{2(p - p_\infty)}{\left(\rho_\infty U_\infty^2\right)}$$

As shown, the pressure response for the $K = 0.8$ case is not affected strongly by the discretization accuracy except near the suction peak and stagnation point, where the second-order prediction is in closer accord with the experimental data. Velocity profiles extracted at $s/d = 2$ for the $K = 0.8$ case (Fig. 7) indicate only slight differences between first- and second-order predictions, an inherent trait of low-diffusion upwind methods for attached flows.

Figures 6, 8, and 9 illustrate the effect of lowering the cavitation number on the flow response. As K decreases, the pressure in the expansion region drops to the vapor pressure, resulting in the generation of a vapor phase and the growth of a cavitation bubble. Pressure recovery farther downstream leads to the collapse of the cavity in a wake region. The structure of the wake region is strongly influenced by both the thermodynamic model and the velocity field, which in itself is influenced by the turbulence model. Some weaknesses of the present approach are evident in comparisons with surface pressure data shown in Figs. 6 and 8. For $K = 0.4$ (Fig. 6) and $K = 0.3$ (Fig. 8), the extent of the bubble is captured properly, but the collapse of the cavity in the wake region is too rapid, leading to a pressure overshoot that is generally larger for the higher-order solutions. This effect, a likely consequence of the assumption of phase

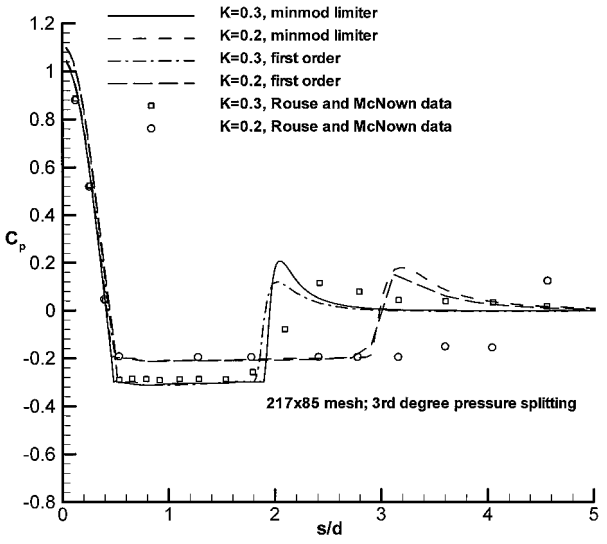

Fig. 8 Surface pressure distributions: $K = 0.2$ and 0.3.

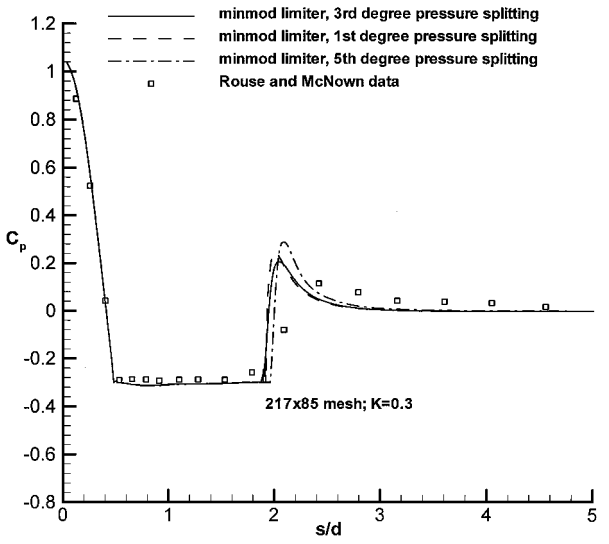

Fig. 10 Effect of pressure splitting on surface pressure distributions: $K = 0.3$.

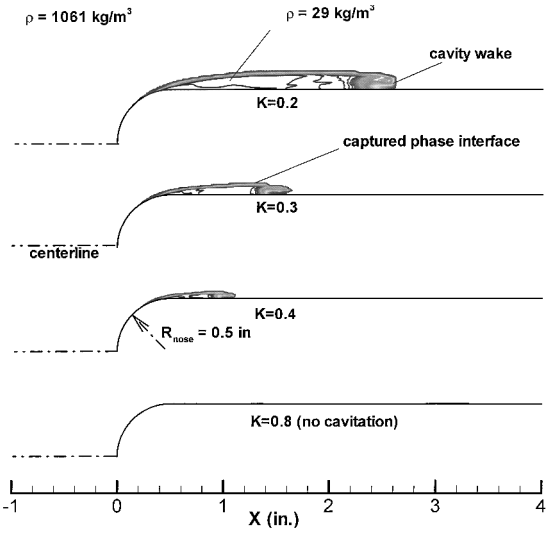

Fig. 9 Density contours: liquid water flow over hemisphere/cylinder geometry.

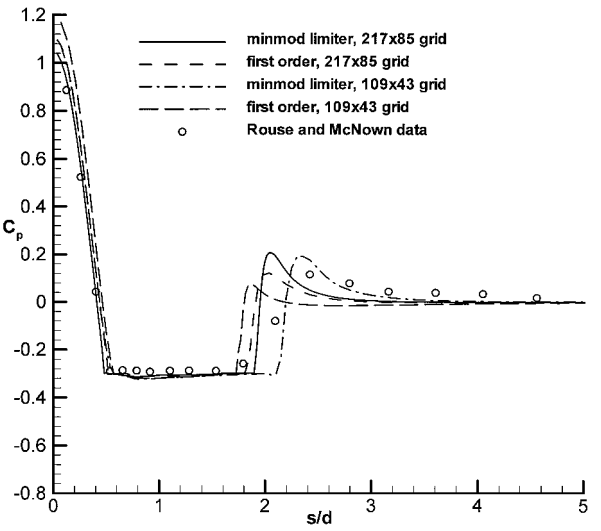

Fig. 11 Effect of mesh refinement on surface pressure distributions: $K = 0.3$.

equilibrium in the wake region, is compounded by the tendency of the upwind scheme to treat the transition from an equilibrium two-phase flow to a single-phase liquid in a shocklike fashion (Fig. 4). The effects of this behavior on the computed density fields (using the minmod limiter) are shown in Fig. 9. The initial vapor–liquid interface is well captured, but the density solution in the wake region exhibits nonsmooth, stair-stepping behavior as points change from being two phase to single phase. Such changes occur continually as the solution progresses, meaning that convergence in the sense of a decreasing residual norm does not result, although bubble lengths eventually stabilize after roughly 4000 iterations at a CFL number of 1.5. This unsteady behavior has been observed in other numerical simulations[38] and mimics, to some extent, physical effects occurring within the wake region.[39] The results for $K = 0.2$ underpredict the bubble size. In addition to the factors mentioned earlier, these results may be influenced by insufficient grid resolution in the collapse region and by large-scale unsteadiness present in the experiment.[35]

Figure 10 illustrates the effect of the degree of polynomials used in the pressure splittings on the solutions for $K = 0.3$. Differences among the predictions are only significant in the cavity wake region, with the fifth-degree splitting resulting in a slightly longer cavity and a larger pressure overshoot. Given the possible inadequacy of the thermodynamic formulation in the wake region and the unsteady behavior already mentioned, these results must be considered inconclusive. The effects of grid refinement on the predictions for $K = 0.3$ are shown in Fig. 11 for both the second-order and first-order discretizations. For the first-order discretization on the coarse 109×43 mesh, the predicted bubble length is slightly less than that obtained for both discretizations on the fine mesh, and the pressure peak following cavity collapse is less pronounced. In contrast, the second-order discretization results in a longer predicted cavity length on the coarse mesh.

Figure 12 displays convergence histories corresponding to the noncavitating ($K = 0.8$) case. As shown, simulations using a both a first-order discretization and a second-order discretization without slope limiting converge roughly five orders of magnitude before roundoff error accumulation halts the residual norm decrease. The effect of minmod slope limiting is to halt the residual decrease after roughly a four-order-of-magnitude drop. This convergence degradation due to roundoff error accumulation is a well-known consequence of integrating the compressible equations at low Mach number, one that may be eliminated through the careful use of gauge pressures and enthalpies.[2,40] Such devices have yet to be tried in the present work. As the convergence degradation typically occurs at residual levels below truncation error, it is generally not a cause for concern. Note that the calculations at lower cavitation numbers do not converge even in this sense due to the unsteady behavior mentioned earlier.

D. Liquid CO_2 Expansion Through a Sharp-Orifice Nozzle

The last test case corresponds to the rapid expansion of liquid carbon dioxide through a reservoir/capillary nozzle system. Devices

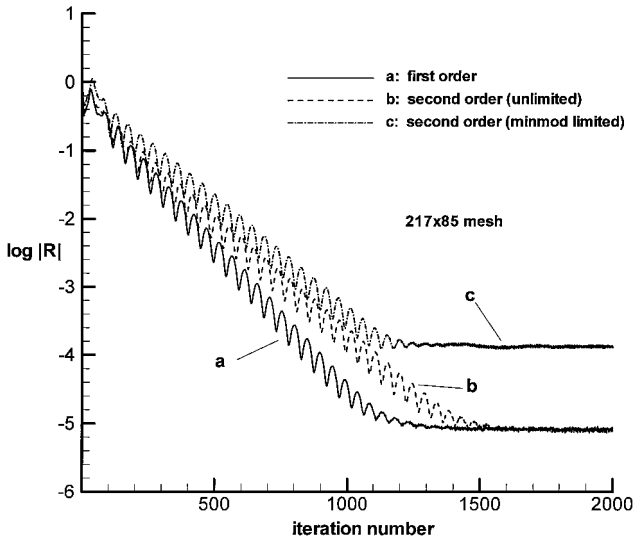

Fig. 12 Convergence histories for noncavitating ($K = 0.8$) liquid water flow over hemisphere/cylinder geometry.

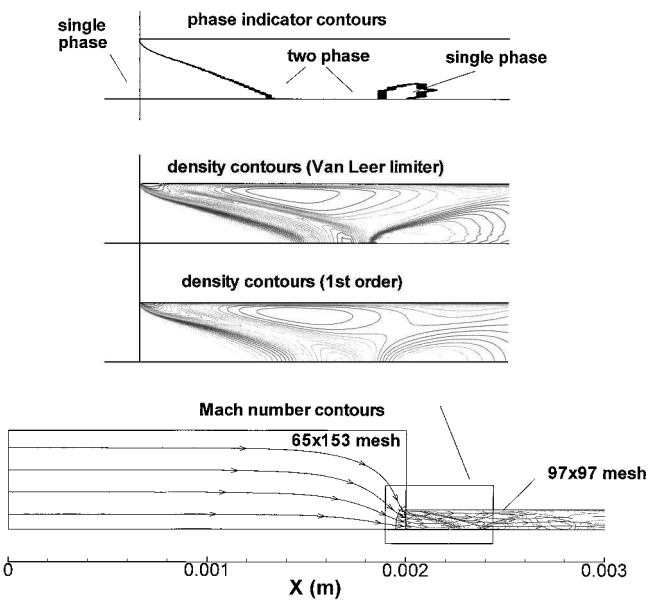

Fig. 13 Mach number, density, and phase indicator contours: liquid CO_2 expansion through a sharp-orifice nozzle.

such as this are being studied as means of depositing solid or liquid substances initially dissolved in liquid or supercritical-fluid carbon dioxide.[41] Figure 13 illustrates Mach number, density, and phase indicator contours in the interior of the nozzle. The phase indicator separates single-phase mesh cells, described by the Sanchez–Lacombe equation,[19] from mesh cells in which the homogeneous equilibrium model is utilized. A two-block grid is employed, with the reservoir block containing 65×153 points and the capillary nozzle block containing 97×97 points. The flow is axisymmetric, and the reservoir total conditions are $p_o = 20.7 \times 10^6$ Pa and $T_o = 300$ K. These conditions place the incoming fluid in the liquid state, but one very near the predicted critical temperature of 304.7 K [Eq. (7)]. As such, a more gasdynamic response of the bulk fluid with rapid expansion might be expected. The inflow boundary conditions fix the total pressure and temperature and extrapolate the u component of velocity from the interior. The expansion of the fluid around the sharp corner is rapid enough to force a smooth transition to the vapor phase, leading to a supersonic flow exiting the nozzle. The initial liquid/two-phase interface coincides with the sonic line and represents a discontinuity in the thermodynamic derivatives. A localized recompression back into a single phase takes place downstream of the point of shock impingement on the centerline. No discontinuity in the bulk fluid properties is evidenced, however, as the transition into the two-phase region takes place very near the critical point of the fluid. Calculations without the equilibrium two-phase flow model were found to be unstable because the rapid expansion drives the fluid density in the corner region below the liquid spinodal value. The pressure values remain reasonable, in contrast to the one-dimensional octane expansion described earlier, but the acoustic speeds become complex. The effects of the Van Leer-limited second-order extension are confined to the orifice region, where the second-order calculation results in crisper predictions of the supersonic flow response. Features of note include regular oblique-shock and Mach wave reflections as well as a small pocket of reversed flow downstream of the corner. The displacement effect of this structure forms an area minimum, allowing the transition to supersonic flow.

VI. Conclusions

Simple modifications for extending the AUSM+ low-diffusion upwind scheme toward the calculation of real fluids at all speeds and at all states of compressibility have been outlined. The real fluid state description is based on the Sanchez–Lacombe equation,[19] although any equation of state could be used in principle. The state description is augmented by a homogeneous equilibrium model for liquid–vapor phase transitions. The proposed modifications utilize time-derivative preconditioning to effect the transition from upwind formulations valid for strongly compressible flows to discretizations valid for nearly incompressible flows. Results indicate that the modifications proposed herein are effective in simulating incompressible liquid and compressible vapor responses as well as multiphase flow phenomena, such as the appearance of cavitation bubbles and vapor–liquid condensation shocks. A point of concern is the robustness of the current procedures in capturing severe phase transitions, a possible consequence of the equilibrium phase change model. Work is underway to improve this behavior. This work provides a starting point for a more comprehensive investigation of upwind discretization techniques for general nonequilibrium multiphase flows. Efforts in this direction are also underway.

Acknowledgments

The work of the first and second authors was supported by the Kenan Center for the Utilization of Carbon Dioxide in Manufacturing, an industry/government/university consortium located at North Carolina State University, and by the NASA John H. Glenn Research Center at Lewis Field through Contract NAS3-97186. Cray T-90 computing time was provided by a grant from the North Carolina Supercomputing Center.

References

[1]Turkel, E., "Preconditioned Methods for Solving the Incompressible and Low Speed Compressible Equations," *Journal of Computational Physics*, Vol. 72, No. 10, 1987, pp. 277–298.

[2]Choi, Y. H., and Merkle, C. L., "The Application of Preconditioning in Viscous Flows," *Journal of Computational Physics*, Vol. 105, No. 4, 1993, pp. 207–223.

[3]Van Leer, B., Lee, W. T., and Roe, P. L., "Characteristic Time Stepping or Local Preconditioning of the Euler Equations," AIAA Paper 91-1552, July 1991.

[4]Weiss, J. M., and Smith, W. A., "Preconditioning Applied to Variable and Constant Density Time-Accurate Flows on Unstructured Meshes," AIAA Paper 94-2209, June 1994.

[5]Oefelein, J. C., and Yang, V., "Simulation and Analysis of Supercritical Multiphase Combustion Processes," AIAA Paper 96-2880, June 1996.

[6]Merkle, C. L., Sullivan, J. Y., Buelow, P. E. O., and Venkateswaran, S., "Computation of Flows with Arbitrary Equations of State," *AIAA Journal*, Vol. 36, No. 4, 1998, pp. 515–521.

[7]Toumi, I., "A Weak Formulation of Roe's Approximate Riemann Solver," *Journal of Computational Physics*, Vol. 102, No. 10, 1992, pp. 360–373.

[8]Toumi, I., and Kumbaro, A., "An Approximate Linearized Riemann Solver for a Two-Fluid Model," *Journal of Computational Physics*, Vol. 124, No. 3, 1996, pp. 286–300.

[9]Coquel, F., El Amine, K., Godlewski, E., Perthame, B., and Rascle, P., "A Numerical Method Using Upwind Schemes for the Resolution of Two-Phase Flows," *Journal of Computational Physics*, Vol. 136, No. 3, 1997, pp. 272–288.

[10]Tang, H. S., and Huang, D., "A Second-Order Accurate Capturing Scheme for 1-D Inviscid Flows of Gas and Water with Vacuum Zones," *Journal of Computational Physics* Vol. 128, No. 10, 1996, pp. 301–318.

[11]Tiselj, I., and Petelin, S., "Modeling of Two-Phase Flow with Second-Order Accurate Scheme," *Journal of Computational Physics*, Vol. 136, No. 9, 1997, pp. 503–521.

[12]Toumi, I., Kumbaro, A., and Paillere, H., "Approximate Riemann Solvers and Flux Vector Splitting Schemes for Two-Phase Flow," 30th Computational Fluid Dynamics Lecture Series Program, von Kármán Inst. for Fluid Dynamics, Rhode-Saint Genese, Belgium, 1999.

[13]Liou, M.-S., "Progress Towards an Improved CFD Method: AUSM+," AIAA Paper 95-1701, June 1995.

[14]Wada, Y., and Liou, M.-S., "A Flux Splitting Scheme with High-Resolution and Robustness for Discontinuities," AIAA Paper 94-0083, Jan. 1994.

[15]Edwards, J. R., "A Low-Diffusion Flux-Splitting Scheme for Navier–Stokes Calculations," *Computers and Fluids*, Vol. 26, No. 6, 1997, pp. 635–657.

[16]Edwards, J. R., and Liou, M.-S., "Low-Diffusion Flux-Splitting Methods for Flows at All Speeds," *AIAA Journal*, Vol. 36, No. 9, 1998, pp. 1610–1617.

[17]Saurel, R., Cocchi, J. P., and Butler, P. B., "Numerical Study of Cavitation in the Wake of a Hypervelocity Underwater Projectile," *Journal of Propulsion and Power*, Vol. 15, No. 4, 1999, pp. 513–522.

[18]Yabe, T., Xiao, F., and Zhang, Y., "Strategy for Unified Solution of Solid, Liquid, Gas, and Plasmas," AIAA Paper 99-3509, June 1999.

[19]Sanchez, I. C., and Lacombe, R. H., "An Elementary Molecular Theory of Classical Fluids: Pure Fluids," *Journal of Physical Chemistry*, Vol. 80, No. 21, 1976, pp. 2352–2362.

[20]Peng, D.-Y., and Robinson, D. B., "A New Two-Constant Equation of State," *Industrial and Engineering Chemistry Fundamentals*, Vol. 15, No. 1, 1976, pp. 59–64.

[21]Edwards, J. R., Franklin, R. K., and Liou, M.-S., "Low-Diffusion Flux-Splitting Methods for Real Fluid Flows at All Speeds," AIAA Paper 99-3327, June 1999.

[22]Liou, M.-S., and Edwards, J. R., "AUSM Schemes and Extensions for Low Mach and Multiphase Flows," 30th Computational Fluid Dynamics Lecture Series Program, von Kármán Inst. for Fluid Dynamics, Rhode-Saint Genese, Belgium, 1999.

[23]Modell, M., and Reid, R. C., *Thermodynamics and Its Applications*, 2nd ed., Prentice–Hall, Englewood Cliffs, NJ, 1983, pp. 154, 155.

[24]McBride, B. J., Gordon, S., and Reno, M. A., "Coefficients for Calculating Thermodynamic and Transport Properties of Individual Species," NASA TM-4513, Oct. 1993.

[25]Brennen, C. E., *Cavitation and Bubble Dynamics*, Oxford Engineering Science Series 44, Oxford Univ. Press, New York, 1995, pp. 163–165.

[26]Liou, M.-S., and Edwards, J. R., "Numerical Speed of Sound and Its Application to Schemes for All Speeds" AIAA Paper 99-3268, June 1999.

[27]Van Leer, B., "Flux-Vector Splitting for the Euler Equations," *Lecture Notes in Physics*, Vol. 170, Springer-Verlag, Berlin, 1982, pp. 507–512.

[28]Liou, M.-S., and Steffen, C. J., "A New Flux Splitting Scheme," NASA TM-104404, May 1991; also *Journal of Computational Physics*, Vol. 107, No. 7, 1993, pp. 23–39.

[29]Edwards, J. R., and Roy, C. J., "Preconditioned Multigrid Methods for Two-Dimensional Combustion Calculations," *AIAA Journal*, Vol. 36, No. 2, 1998, pp. 185–192.

[30]Olchowny, G. A., and Sengers, J. V., "Crossover from Singular to Regular Behavior of the Transport Properties of Fluids in the Critical Region," *Physical Review Letters*, Vol. 61, No. 1, 1988, pp. 15–18.

[31]Lide, D. R., and Kehiaian, H. V., *CRC Handbook of Thermophysical and Thermochemical Data*, CRC Press, Boca Raton, FL, 1994, pp. 329, 418.

[32]Spalart, P. R., and Allmaras, S. R., "A One-Equation Turbulence Model for Aerodynamic Flows," AIAA Paper 92-0439, June 1992.

[33]Ransom, V. H., *Numerical Benchmark Tests*, edited by G. F. Hewitt, J. M. Delhay, and N. Zuber, Vol. 3, Multiphase Science and Technology, Hemisphere, Washington, DC, 1987, pp. 465–467.

[34]Shu, C.-W., and Osher, S., "Efficient Implementation of Essentially Non-Oscillatory Shock Capturing Schemes," *Journal of Computational Physics*, Vol. 77, No. 8, 1988, pp. 439–471.

[35]Rouse, H., and McNown, J. S., "Cavitation and Pressure Distribution: Head Forms at Zero Angle of Yaw," State Univ. of Iowa Engineering Bulletin 32, Ames, IA, 1948.

[36]Deshpande, M., Feng, J., and Merkle, C. L., "Nonlinear Euler Analysis of 2-D Cavity Flow," *Cavitation and Multiphase Flow Forum*, FED-Vol. 135, American Society of Mechanical Engineers, Fairfield, NJ, 1992.

[37]Chen, Y., and Heister, S. D., "A Numerical Treatment of Attached Cavitation," *Journal of Fluids Engineering*, Vol. 116, No. 9, 1994, pp. 613–618.

[38]Chen, Y., and Heister, S. D., "Modeling Hydrodynamic Non-Equilibrium in Bubbly and Cavitating Flows," *Journal of Fluids Engineering*, Vol. 118, No. 1, 1995, pp. 172–178.

[39]Ceccio, S. L., and Brennen, C. E., "Dynamics of Attached Cavities on Bodies of Revolution," *Journal of Fluids Engineering*, Vol. 114, No. 3, 1991, pp. 93–99.

[40]Fiterman, A., Turkel, E., and Vatsa, V., "Pressure Updating Methods for the Steady State Fluid Equations," AIAA Paper 95-1652, June 1995.

[41]Matson, D. W., Fulton, J. L., Peterson, R. C., and Smith, R. D., "Rapid Expansion of Supercritical Fluid Solutions: Solute Formation of Powders, Thin Films, and Fibers," *Industrial and Engineering Chemistry Research*, Vol. 26, No. 11, 1987, p. 2298.

P. Givi
Associate Editor